



OPEN

Resonant Raman scattering of few layers CrBr₃

Łucja Kipczak¹✉, Arka Karmakar¹, Magdalena Grzeszczyk², Róża Janiszewska³, Tomasz Woźniak⁴, Zhaolong Chen^{2,5}, Jan Pawłowski¹, Kenji Watanabe⁶, Takashi Taniguchi⁷, Adam Babiński¹, Maciej Koperski^{2,8} & Maciej R. Molas¹

We investigate the vibrational and magnetic properties of thin layers of chromium tribromide (CrBr₃) with a thickness ranging from three to twenty layers (3–20 L) revealed by the Raman scattering (RS) technique. Systematic dependence of the RS process efficiency on the energy of the laser excitation is explored for four different excitation energies: 1.96 eV, 2.21 eV, 2.41 eV, and 3.06 eV. Our characterization demonstrates that for 12 L CrBr₃, 3.06 eV excitation could be considered resonant with interband electronic transitions due to the enhanced intensity of the Raman-active scattering resonances and the qualitative change in the Raman spectra. Polarization-resolved RS measurements for 12 L CrBr₃ and first-principles calculations allow us to identify five observable phonon modes characterized by distinct symmetries, classified as the A_g and E_g modes. The evolution of phonon modes with temperature for a 16 L CrBr₃ encapsulated in hexagonal boron nitride flakes demonstrates alterations of phonon energies and/or linewidths of resonances indicative of a transition between the paramagnetic and ferromagnetic state at Curie temperature ($T_C \approx 50$ K). The exploration of the effects of thickness on the phonon energies demonstrated small variations pronounced exclusively for the thinnest layers in the vicinity of 3–5 L. We propose that this observation can be due to the strong localization in the real space of interband electronic excitations, limiting the effects of confinement for resonantly excited Raman modes to atomically thin layers.

The recent discovery of magnetism in two-dimensional van der Waals (vdW) materials at the limit of atomically thin monolayers opens capabilities to study the fundamental aspects of magnetism at varied dimensionalities. From the practical perspective, the realization of magnetism down to monolayers pushes the limits of device miniaturization, which becomes increasingly relevant for the development of spintronics^{1,2}, valleytronics, and nanoelectronics^{3–5}. The family of layered magnetic materials (LMMs) grows rapidly motivated by the search for materials that host stable magnetic orders under a variety of physical conditions, including temperature^{6–8}, magnetic or electric field^{7,9,10}, and pressure¹¹. These intense research efforts lead to theoretical predictions of hundreds of LMM systems, of which dozens have been synthesized and characterized. The largest groups of LMMs include di- and trihalides (e.g., CrBr₃ and CrI₃)^{12,13}, transition metal dichalcogenides (e.g., 1T-VS₂)^{14,15}, tri- and tetrachalcogenides (e.g. FePS₃ and CrPS₄)^{16–21}, and metal-chalcogen-halides (e.g., CrSBr)^{22,23}.

Herein, we investigate the vibrational properties of CrBr₃, which belongs to the family of chromium trihalides (CrX₃, X = I, Br, Cl). These three materials exhibit an intralayer ferromagnetic coupling within a monolayer, but they differ in the easy-axis magnetization exhibiting in-plane (CrCl₃)^{24,25} or out-of-plane spin orientations (CrBr₃^{26,27} and CrI₃^{28,29}). In their bulk form, two types of magnetic coupling between consecutive layers are apparent, *i.e.*, ferromagnetic in CrBr₃^{26,27} and antiferromagnetic in CrCl₃^{24,25} and CrI₃^{28,29}. However, the interlayer couplings in CrX₃ materials were found to be more complex, displaying thickness- and/or gate-dependent ferromagnetic or antiferromagnetic characteristics^{3,12,28–30}. For CrBr₃, the interlayer coupling is mostly ferromagnetic, however, contributions from antiferromagnetic coupling have been observed in bulk crystals via inspection of magneto-resistance in vertical tunneling junctions³¹.

¹Faculty of Physics, Institute of Experimental Physics, University of Warsaw, 02-093 Warsaw, Poland. ²Institute for Functional Intelligent Materials, National University of Singapore, Singapore 117544, Singapore. ³Department of Semiconductor Materials Engineering, Faculty of Fundamental Problems of Technology, Wrocław University of Science and Technology, 50-370 Wrocław, Poland. ⁴Faculty of Physics, Institute of Theoretical Physics, University of Warsaw, 02-093 Warsaw, Poland. ⁵School of Advanced Materials, Shenzhen Graduate School, Peking University, Shenzhen 518055, China. ⁶Research Center for Electronic and Optical Materials, National Institute for Materials Science, 1-1 Namiki, Tsukuba 305-0044, Japan. ⁷Research Center for Materials Nanoarchitectonics, National Institute for Materials Science, 1-1 Namiki, Tsukuba 305-0044, Japan. ⁸Department of Materials Science and Engineering, National University of Singapore, Singapore 117575, Singapore. ✉email: lucja.kipczak@fuw.edu.pl

From the perspective of studying lattice dynamics, the Raman scattering (RS) technique has been established as a pivotal tool to uncover the physics of the vibrational and electronic properties of layered vdW materials, as well as a method to identify the exact number of layers^{32–35}. Particularly, the RS characterization of CrBr₃ revealed a chiral character of the lattice excitations in a rather complex elementary cell⁸. These phonon modes are coupled to the magnetic order, predominantly driven by modifications of the exchange coupling between neighboring Cr³⁺ ions due to vibrational motion of the lattice³⁶.

In this work, we further explore the interplay between vibrational, electronic, and magnetic characteristics of thin CrBr₃ layers through systematic polarization-resolved RS characterization as a function of the energy of laser excitation, temperature, and the thickness of the magnetic layers. We concluded that for 12 L CrBr₃ 3.06 eV excitation energy creates resonant conditions characterized by enhanced RS efficiency at the cryogenic temperature $T = 5$ K. Five Raman peaks were identified in the polarization-sensitive resonant RS spectra, characterized by the A_g (out-of-plane) and E_g (in-plane) symmetries, as confirmed by first-principles calculations. Curie temperature (T_C) for CrBr₃ is determined to be ~ 50 K from the measured sudden energy redshift of the Raman resonances triggered by the increase of temperature above the critical point, at which the ferromagnetic order collapses in favor of the paramagnetic response. Moreover, the effect of thicknesses on the phonon energies reveals a notable change in phonon energy only for the thinnest layers (3–5 L CrBr₃), indicative of the strong spatial localization of excitons³⁷ which are expected to be responsible for the resonant characteristics of the enhanced vibrational response.

Results and discussion

Crystal structure of CrBr₃

CrBr₃ crystallizes in a rhombohedral BI₃ structure of $R\bar{3}$ symmetry. The schematic representation of the atomic structure of the CrBr₃ crystal is shown in Fig. 1. Within each layer, Cr atoms form a hexagonal crystal lattice, with each atom bonded to its six neighboring Br atoms, forming an octahedral configuration. The CrBr₃ layers are stacked along the c axis and are held together by vdW interactions^{38–40}. CrBr₃ crystal exhibits the rhombohedral arrangement at low and ambient temperatures^{36,41}, unlike its counterparts, CrI₃ and CrCl₃, which undergo a structural transition from the monoclinic AlCl₃ phase of C2/m symmetry at ambient temperature towards rhombohedral $R\bar{3}$ structure at low temperature. The transition was identified to occur at 210 K and 240 K for CrI₃ and CrCl₃, respectively^{24,42}. The rhombohedral primitive cell belongs to space group no. 148 with Cr and Br atoms in $6c$ and $18f$ Wyckoff positions, respectively. It gives rise to eight Raman-active modes, classified as: $\Gamma = 4A_g + 4E_g$, where the E_g modes are doubly degenerate^{36,41,43}. We calculated the dispersion of the phonon modes for bulk CrBr₃ in the presence of ferromagnetic order in the density functional theory (DFT) framework, as illustrated in Fig. 2. The superscripts in the labels of the peaks describe additional numbering due to their increased Raman shift. The optimized lattice constant of rhombohedral cell, $a = 7.128$ Å, corresponds to $a = 6.352$ Å in hexagonal cell, in good agreement with the experimental value of 6.302 Å⁴¹.

Resonant conditions of Raman scattering in CrBr₃

The representative low temperature ($T = 5$ K) unpolarized RS spectra of a mechanically exfoliated 12 L CrBr₃ deposited on Si/SiO₂ substrate are demonstrated in Fig. 3a. We comparatively inspect the dependence of the RS resonances on the laser energy, utilizing 1.96 eV, 2.21 eV, 2.41 eV, and 3.06 eV excitations. There are five distinct RS peaks in the spectra, and these peaks can be attributed to the in-plane E_g and out-of-plane A_g modes^{8,36,41,43,44}. Specifically, four phonon modes, apparent at 110 cm⁻¹ (A_g²), 146 cm⁻¹ (E_g²), 156 cm⁻¹ (E_g³), and 187 cm⁻¹ (A_g³), are observed under all the used excitation energies, while the fifth one at 282 cm⁻¹ (E_g⁴) is seen exclusively when excited with a 3.06 eV energy. DFT calculations yield frequencies of 110 cm⁻¹, 137 cm⁻¹, 142 cm⁻¹, 177 cm⁻¹

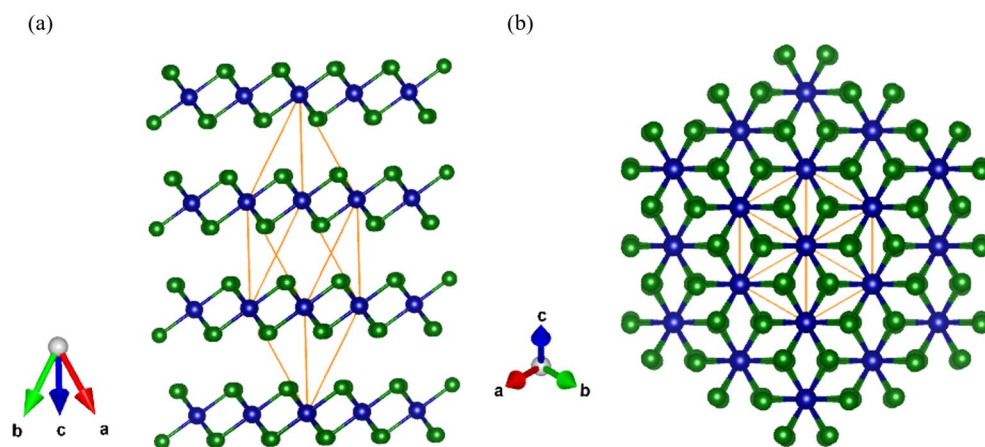


Figure 1. The schematic representation of (a) a side view and (b) a top view the atomic structure of the CrBr₃ crystal in rhombohedral configuration. The orange parallelepiped represents the unit cell, which consists of three molecular layers including two Cr atoms (blue) and six Br atoms (green) per layer.

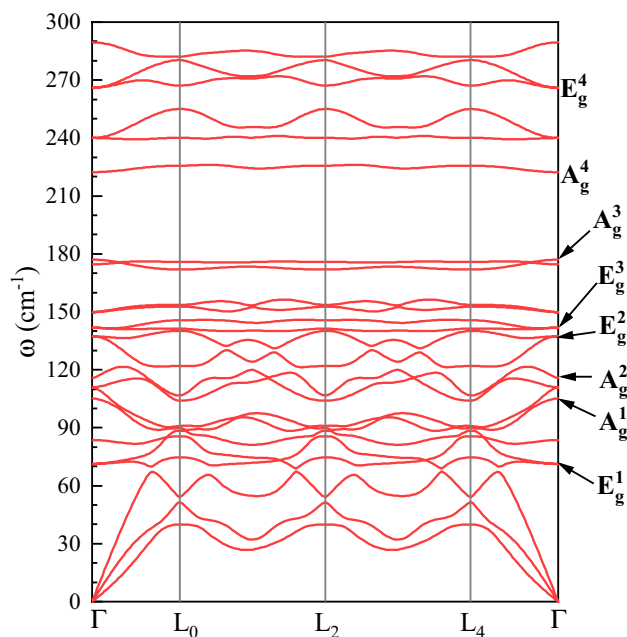


Figure 2. Phonon dispersion of bulk CrBr₃ crystal in rhombohedral primitive cell with ferromagnetic order. The Γ point corresponds to the center of the Brillouin zone.

and 266 cm^{-1} , respectively, which agree well with the experimentally determined values. We also measured polarization-resolved Raman spectra of the 12 L CrBr₃ flake in two configurations of linearly polarized excitation and detection: co- (solid light blue curve) and cross-linear (dashed dark pink curve), see Fig. 3b. As is shown in Fig. 2, phonon modes in CrBr₃ at the Γ point exhibit E_g and A_g characters. Consequently, the scattering resonances are apparent in both co- and cross-linear configurations (E_g) or only in the co-linear one (A_g). The spectra, resolved by the linear polarization demonstrated in Fig. 3b, are consistent with the aforementioned symmetry analysis of the phonon modes. Note that the observation of the A_g^3 mode in the cross-linear alignment likely originates from the resonant excitation conditions of RS. The coupling with an exciton can modify the polarization properties of the scattering resonances in the RS experiment.

The intensities of the phonon resonances change with the variation of the excitation energy, see Fig. 3a. The smallest intensity of all observed Raman modes occurs at an excitation energy of 1.96 eV. Intermediate intensities were observed for excitation energies of 2.21 eV and 2.41 eV. Finally, the highest intensities for the E_g^2 , E_g^3 , and A_g^3 modes are seen under excitation of 3.06 eV, but simultaneously the A_g^2 intensity is smaller as compared to the 2.21 eV and 2.41 eV excitations. A similar variation in the intensity of the RS spectra under different excitations was reported in Ref.³⁶, where the Raman spectra of the CrBr₃ monolayer were investigated using two different excitation energies, *i.e.*, 1.65 eV and 2.09 eV. Similar trend representing the modifications of the E_g^4 mode intensity was indicative of a strong dependence on the applied excitation energy.

It is well established that the intensity of the RS signal in vdW materials is significantly dependent on the excitation energy⁴⁵. In the simplest approach, the resonant conditions of RS, related to the electron-phonon coupling in a material, occur when the excitation energy of the RS processes is in the vicinity of a given transition (*e.g.* electronic or excitonic) in the material⁴⁶. To identify possible transitions involved in the resonant conditions of RS in CrBr₃, we measured photoluminescence excitation (PLE) spectrum by probing the broad photoluminescence (PL) band of bulk CrBr₃ under continuously modified laser energy, see Fig. 3c. The PL spectrum of the CrBr₃ bulk is characteristic for the molecular crystal, where excitons are localized on individual molecules (Frenkel type) and its recombination follows the Frank-Condon principle, as previously reported in Ref.³⁷. The corresponding PLE spectrum is composed of three broad transitions centered at about 1.68 eV, 2.16 eV, and 2.65 eV, and an increase in the absorption strength can be observed at energies higher than about 2.9 eV. These peaks coincide with three significant resonances apparent at energies of about 1.7 eV, 2.2 eV, and 3.0 eV, reported in experimental low temperature ($T \sim 2 - 4$ K) absorption spectra of CrBr₃^{26,27,47-50} and in the corresponding theoretical predictions of the imaginary part of the dielectric function⁵¹. The colored lines indicated in the PLE spectrum represent the excitation energies of lasers used for RS measurements. In particular, there are no absorption resonances at excitations of 1.96 eV and 2.41 eV, while the 2.21 eV and 3.06 eV laser energies occur at spectral ranges of significant absorption strength. Except for 2.41 eV energy, the PLE spectrum of the CrBr₃ bulk can qualitatively explain the resonant excitation conditions of Raman scattering, suggesting the influence of the excited states of the Frenkel exciton on the electron-phonon coupling in CrBr₃. The most challenging is the qualitative description of the Raman spectrum intensity under 2.41 eV excitation. The studies of the resonant Raman conditions in thin layers of transition metal dichalcogenides reveal that resonant cases can not be explained only by coincidence between the laser energy and the maximum of electronic density

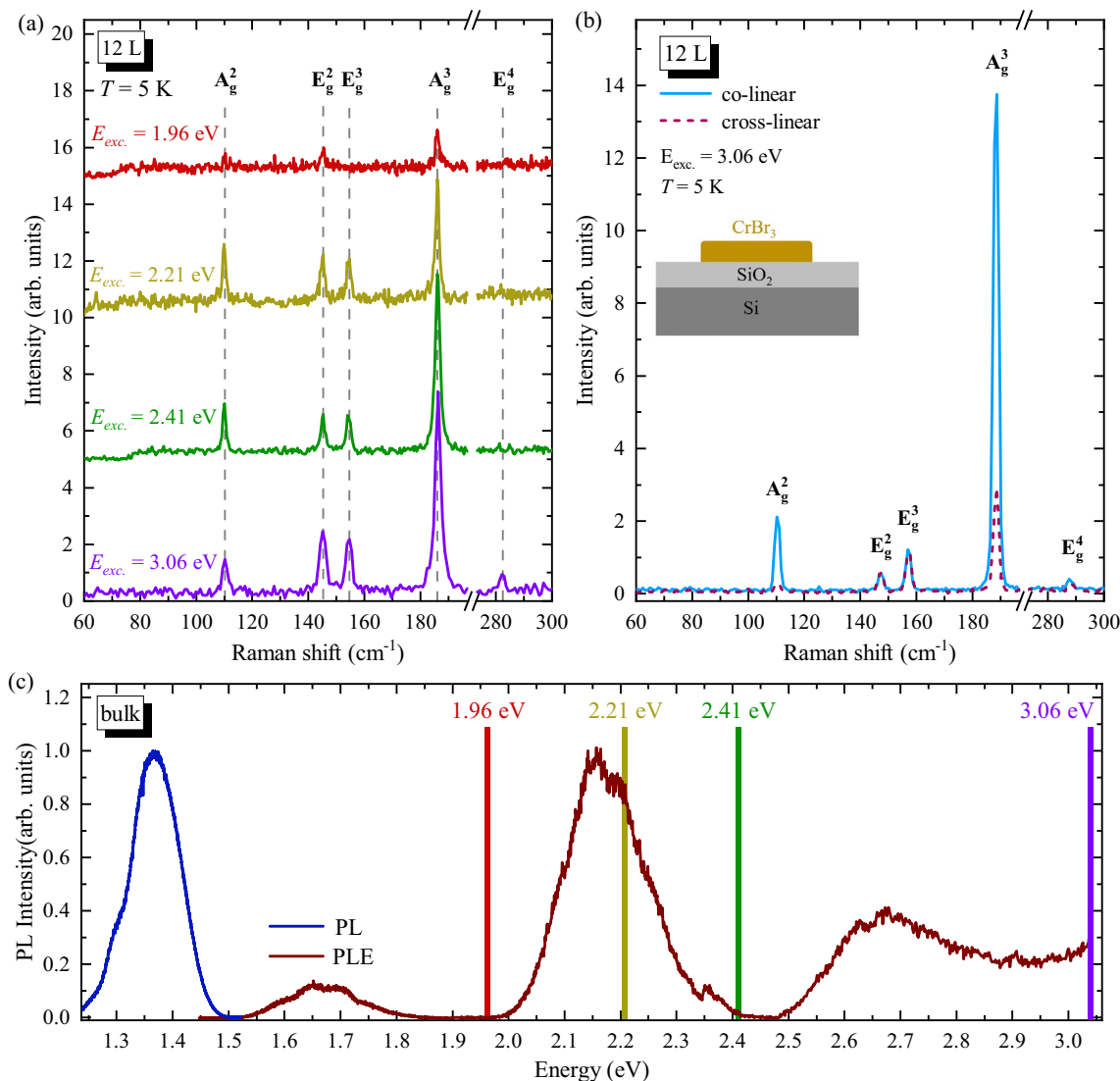


Figure 3. (a) Raman Scattering (RS) spectra of 12 L of CrBr₃ measured at 5 K with different excitation energies: 1.96 eV, 2.21 eV, 2.41 eV and 3.06 eV, using excitation power 50 μ W. Spectra were shifted vertically for better visual representation. (b) Low-temperature ($T = 5$ K) RS spectra of the same flake, but at different spatial location, measured in co- (light-blue) and cross-linear (dashed dark pink) configurations of polarized light using 3.06 eV excitation energy and power 50 μ W. Insert represents a schematic illustration of the sample cross-section. (c) Low-temperature ($T = 1.6$ K) PL (dark-blue) and PLE (brown) spectra of bulk CrBr₃. Lines in different colors have been plotted on the PLE spectra to represent the laser excitation energies in RS experiments.

states⁵², but it requires sophisticated calculations of impacts of all transitions from the whole Brillouin zone to the electron-phonon coupling⁵³. We believe that our results will motivate the development of theoretical models to describe the exciton-phonon interaction in chromium trihalides.

Temperature effect on phonon modes in CrBr₃

Most LMMs undergo different types of degradation, such as photocatalysis and photochemical or photothermal oxidation, which are substantially dependent on various factors such as light exposure and temperature^{54–60}. It has been reported that CrCl₃ is the most stable CrX₃ material in ambient conditions^{57,61}, while the degradation processes increase for CrBr₃⁵⁹, and CrI₃ is the most unstable chromium trihalide⁵⁴. During our investigation, we also observed that exfoliated thin CrBr₃ flakes on Si/SiO₂ substrates are subjected to the degradation process under laser illumination, particularly at higher temperatures, close to room temperature. Therefore, we performed the temperature-dependent RS spectra on 16 L flake encapsulated in hBN layers, and the structure was also covered by a thin layer of optically inactive polymer to add additional protection (see section “Methods” for details) against degradation (see Fig. 4a). The temperature evolution of the Raman spectra of the CrBr₃ flake is presented in Fig. 4b. Note, that we were able to carry out the measurements only up to 200 K due to the degradation caused by the elevated temperature. There are three effects of the increased temperature on a

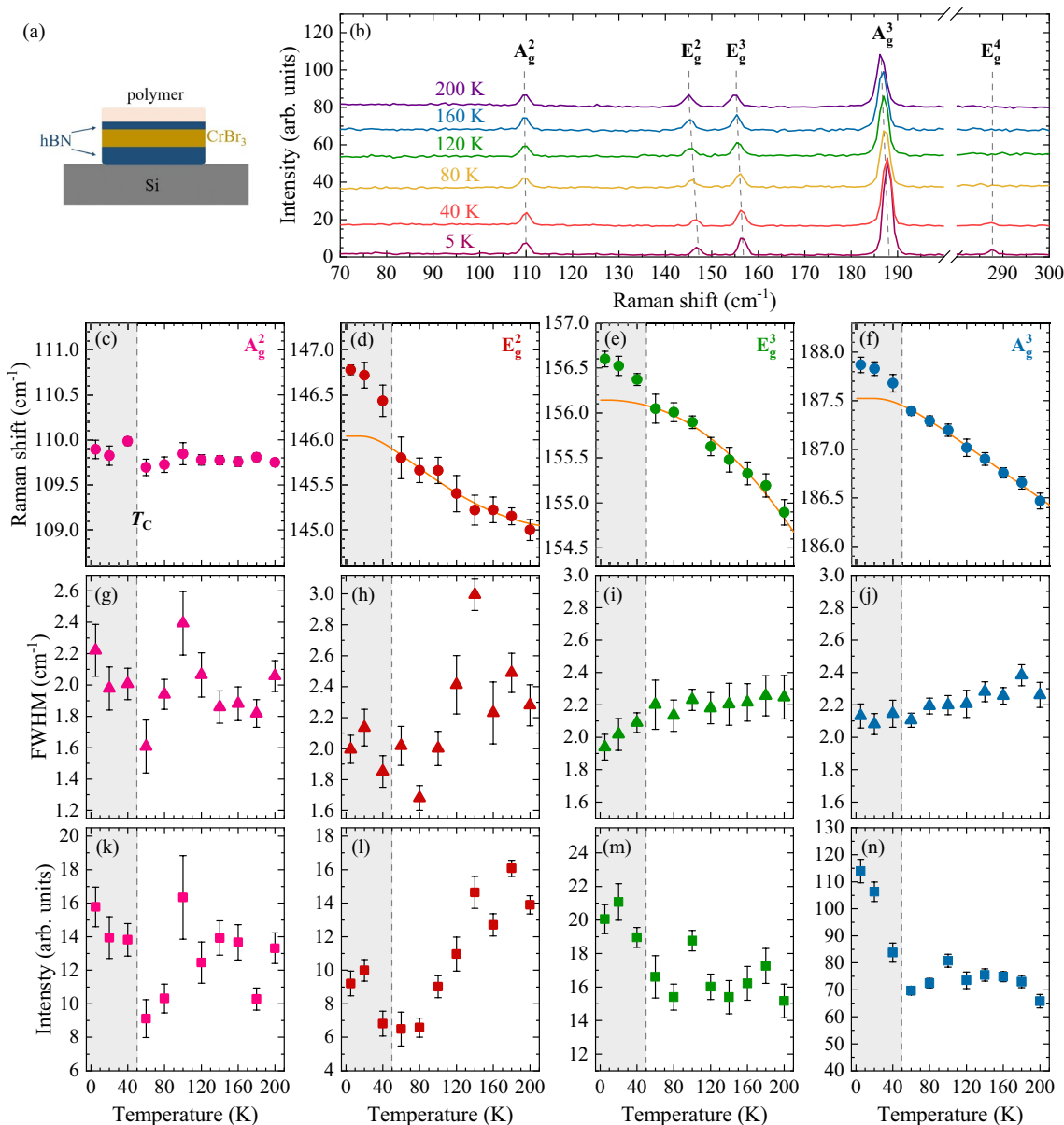


Figure 4. (a) Schematic representation of the investigated sample. The 16 L flake of CrBr₃ was encapsulated in hBN and coated with an optically inactive polymer and placed on silicon substrate. (b) Temperature evolution of RS spectra of CrBr₃ measured at selected temperature between 5 and 200 K under the 3.06 eV excitation and $P=100\ \mu\text{W}$. Temperature dependence of (c)–(f) Raman shifts, (g)–(j) FWHMs and (k)–(n) integrated intensities obtained of the A_g², E_g², E_g³, and A_g³ phonon modes. The errors are indicated by black bars. The shaded grey rectangle represents the ferromagnetic region, while the border delineates the Curie temperature (T_C).

given Raman peak that are revealed: red shift of energy, broadening of linewidth, and variation of intensity. To investigate the temperature effect in more detail, we fitted the observed phonon modes with Lorentzian functions. The obtained temperature evolutions of the peak energies, full widths at half maximum (FWHMs), and intensities for four phonon modes, *i.e.*, A_g², E_g², E_g³, A_g³, are shown in Fig. 4c–f, (g)–(j), and (k)–(n), respectively.

While the Raman shift of the A_g² mode is relatively insensitive to temperature changes, three other modes (E_g², E_g³, and A_g³) gradually redshift with increasing temperature. Especially, in between 40 and 60 K the energies undergo significant redshifts, followed by nearly linear decreases at higher temperatures. These abrupt reductions were observed in the literature and identified as a fingerprint of the transition from the ferromagnetic phase at low temperature to the paramagnetic phase at higher temperatures^{8,36,41,43}. We estimate the Curie temperature (T_C) for CrBr₃ to be around 50 K. The determined value of T_C is in very good agreement with the recent result obtained for the exfoliated CrBr₃ flake (47 K⁸), but is much bigger value as compared to the one for as-grown crystal (33 K²⁷ and 27 K⁴¹) or in a monolayer limit (25 K³⁶). The T_C difference between the exfoliated flakes and the as-grown crystal of CrBr₃ can be explained by the influence of stress on the magnetic interactions between atoms, which probably leads to a modulation of the transition temperature between the ferromagnetic and paramagnetic phases⁶².

Typically, the temperature evolution of phonon energies can be described using the anharmonic model proposed in Ref.⁶³, which reads:

$$\omega(T) = \omega_0 + A \left(1 + \frac{2}{e^x + 1} \right) + B \left(1 + \frac{3}{e^y - 1} + \frac{3}{(e^y - 1)^2} \right) \quad (1)$$

where the ω_0 , A , and B are fitting parameters, $x = \frac{\hbar\omega_0}{2k_B T}$, $y = \frac{\hbar\omega_0}{3k_B T}$ and $\omega_0 + A + B$ is the phonon frequency at 0 K.

As can be seen in Fig. 4d–f, this model can characterize the phonon temperature dependences, but only for temperature higher than T_C . At $T < T_C$ the phonon energies are significantly larger than those predicted by the model. The reason for this aspect is the spin-phonon coupling caused by ionic motions⁴¹. The spin-phonon coupling coefficient can be given by the formula^{8,64–66}:

$$\omega(T) \sim \omega_{anh}(T) + \lambda \langle S_i \cdot S_j \rangle \quad (2)$$

where $\omega(T)$ represents the measured phonon energy, $\omega_{anh}(T)$ denotes the phonon energy without spin-phonon coupling, λ denotes the coupling strength, $\langle S_i \cdot S_j \rangle$ is the spin-spin correlation function of neighboring spins, and the values of S_i and S_j are $3/2$ ^{8,67,68}. The obtained λ values for the ω_{anh} (60 K) are 0.43 cm^{-1} , 0.24 cm^{-1} , and 0.21 cm^{-1} correspondingly for the E_g^2 , E_g^3 , and A_g^3 modes. These values agree with the previously reported data for CrBr_3 at 70 K ⁸.

We also observe a highly disordered dependence of the FWHMs on temperature for the A_g^2 and E_g^2 modes, whereas the corresponding dependences for E_g^3 , and A_g^3 are monotonic with their slow growth at higher temperatures. There is no significant signature of the ferro-to-paramagnetism transition in the temperature evolutions of the FWHMs, in contrast to the results reported in Refs.^{8,41}. Kozlenko et al.⁴¹ demonstrated that the mode linewidths are reduced within the ferromagnetic phase, reaching a minimum at T_C and are followed by their monotonic growth at higher temperatures. On the other hand, Yin et al.⁸ showed similar linewidth behaviors, but the minimum of phonon FWHMs was identified at lower temperature than T_C . Our results accompanied by the literature^{8,41} indicate that the analysis of the phonon linewidths in CrBr_3 is burdened with greater uncertainty in assigning the Curie temperature.

The analysis of the temperature dependence of the phonon intensities is the most intriguing, as there can be two competing transition processes: non-resonant versus resonant conditions of RS excitation and ferro- versus paramagnetic order. The intensities of the A_g^2 and E_g^3 modes exhibit a seemingly stochastic distribution, while the ones corresponding to the E_g^2 and A_g^3 are described by more organized trends. Particularly, the A_g^3 intensity is reduced of about 40% between 5 and 50 K, and then its intensity stabilizes at an almost fixed level. This result indicates that the intensity can also be used to distinguish the transition temperature between different magnetic phases, as reported for other LMMs, e.g., CrSBr ⁶⁹ and $\text{Cr}_2\text{Ge}_2\text{Te}_6$ ⁷⁰.

Thickness-dependent Raman scattering spectra of CrBr_3

The final part of our work is devoted to the examination of the thickness influence on the RS spectra of thin CrBr_3 exfoliated on the Si/SiO_2 substrates. We investigate 25 flakes with thicknesses ranging from 3 to 20 L. Knowing that CrBr_3 degradation is quite slow in the ambient atmosphere, compared to its photocatalytic oxidation⁵⁹, the flakes thicknesses were determined using the AFM technique and then subjected to Raman spectroscopy characterization. Figure 5a,b show the optical and atomic force microscopy (AFM) images of the selected CrBr_3 flake, respectively. Its thickness is estimated to be about 5 nm (see Fig. 5c), which corresponds to 8 L (the experimental thickness of a single layer of CrBr_3 equals 6 \AA ⁵⁰). Figure 5d presents the thickness dependence of the Raman shifts of four phonon modes. The open points represent the phonon energies measured for the individual flakes, characterized by different thickness whereas the solid points denote the mean values calculated for a particular layer thickness. A discernible tendency of the phonon energies as a function of the layer thickness is apparent in the figure. However, the dependence of the Raman shifts, which ranges only from 0.4 to 0.8 cm^{-1} in the investigated range of thicknesses, is hidden by their substantial random variations also within the same number of layers. To better visualize the thickness effect, Fig. 5e illustrates the energy differences between the most prominent A_g^3 peak and others (A_g^2 , E_g^2 , and E_g^3). The observed dependences can be divided into two groups: 3–5 L and 6–20 L. While an evident reduction in the energy difference between the A_g^3 and E_g (E_g^2 and E_g^3) modes is observed when the number of layers increases from 3 to 5 layers, there is no similar behavior for the two A_g peaks (A_g^2 and A_g^3). For the 6–20 L range, all the energy differences between the phonon modes are not affected by the thickness and stay almost at the same level. Our results, shown in Fig. 5, are in agreement with the thickness dependences previously observed for thin layers of transition metal dichalcogenides, e.g. MoS_2 ^{32,71}, MoTe_2 ^{33,72}, and ReSe_2 ³⁴. The energy differences between the A_g and E_g modes are established to be the result of the interaction of the interlayer and surface effects^{71,72}. In the case of thin layers of other CrX_3 , i.e. CrCl_3 ^{73,74} and CrI_3 ⁶, the thickness evolutions of phonon modes were also investigated. For CrCl_3 , a significant difference in Raman shifts between 1–3 L and the bulk was theoretically predicted⁷³, but was not observed in experiments⁷⁴. Although substantial shifts in magnon modes as a function of layers thicknesses were reported in CrI_3 in the limit below 12 layers⁶. Or results may be indicative of the strong spatial localization of excitons³⁷, which are expected to be responsible for the resonant characteristics of the enhanced vibrational response.

Summary

The vibrational and magnetic properties of the thin layers of CrBr_3 were investigated using Raman scattering spectroscopy. We found that the resonant RS for CrBr_3 is observed at low temperature under the 3.06 eV excitation, in agreement with absorption bands revealed by photoluminescence excitation spectroscopy. Furthermore, the temperature dependence of the phonon energies in a 16 L CrBr_3 encapsulated film in hBN

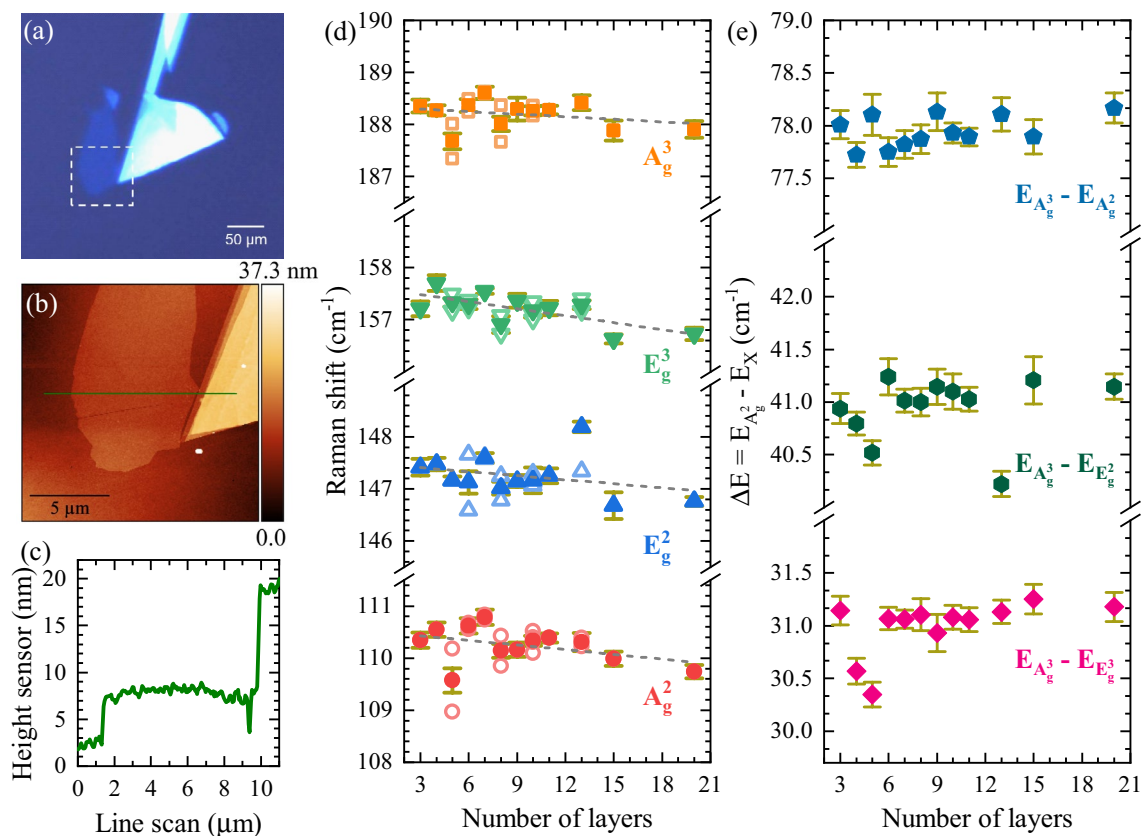


Figure 5. (a) Optical image of 8 L flake of CrBr_3 . Dashed white cube corresponds to an area scanned using atomic force microscopy (AFM). (b) AFM image of the flake. A horizontal line represents the (c) height profile of this flake. (d) Raman shift as a function of number of layers. The solid points represent the average Raman shift values, while the open, lighter points correspond to values of Raman shift for each layer. The errors are indicated by dark yellow bars. (e) Energy difference between the most prominent A_g^2 Raman mode and the remaining modes. The errors are indicated by dark yellow bars.

flakes was analyzed to determine its Curie temperature of about 50 K. Finally, it was established that the effect of thickness on the phonon energies is pronounced only for the thinnest layers in the atomically-thin regime of 3 to 5 layers of CrBr_3 .

Methods

Samples preparation

In the case of initial studies and thickness evolution, thin flakes of CrBr_3 obtained by polydimethylsiloxane (PDMS)-based exfoliation from bulk crystal and then stacked on SiO_2/Si substrates with a thickness of 90 nm or 300 nm of SiO_2 using an all-dry deterministic stamping technique to avoid glue residues⁷⁵. For temperature-dependent and photoluminescence excitation (PLE) measurements, we used samples prepared from a CrBr_3 flake and hBN flakes that were exfoliated directly on a 285 nm SiO_2/Si substrate in an inert gas glovebox (O_2 1 ppm, H_2O < 1 ppm). Then, a poly(bisphenol A carbonate)/polydimethylsiloxane, referred to as a polymer stamp, was used to pick up 50 nm hBN, 10 nm CrBr_3 and 50 nm hBN, respectively at 80 °C with the assistance of the transfer stage in the glovebox. The polymer was left on the structure for protection. CrBr_3 flakes of interest were first identified by visual inspection under an optical microscope and then subjected to atomic force microscopy to obtain their thickness. Bulk CrBr_3 crystals were purchased from HQ Graphene.

Raman scattering spectroscopy

Raman scattering spectra were measured under laser excitations of diode lasers from the Cobolt ($\lambda = 405$ nm (3.06 eV), $\lambda = 515$ nm (2.41 eV), $\lambda = 561$ nm (2.21 eV)), and of He-Ne laser from the Thorlabs ($\lambda = 633$ nm (1.96 eV)) on samples placed on a cold finger of a continuous-flow cryostat, which allows experiments to be carried out as a function of temperature from about 5 K to room temperature. The excitation light was focused by means of a 50× long-working-distance objective with a 0.55 numerical aperture (NA) producing a spot of about 1 μm diameter. The signal was collected via the same objective (backscattering geometry), sent through a 0.75 m spectrometer from the Teledyne Princeton Instruments equipped with 1800 grooves/mm, and then detected using a liquid nitrogen-cooled charge-coupled device (CCD). The laser light was filtered using longpass filters (515 nm, 561 nm, and 633 nm) or a set of Bragg-grating Notch filters (405 nm). The polarization-resolved Raman spectra were analyzed by a motorized half-wave plate and a fixed linear polarizer mounted in the detection path.

Photoluminescence excitation technique

The PLE measurements were performed with a broadband supercontinuum light source with spectral filtering by a monochromator producing a monochromatic beam with a linewidth of about 2 nm. The power on the sample was stabilized by an electrically controlled liquid crystal followed by a linear polarizer acting in a feedback loop with a photodiode monitoring the laser power entering into the probe. The CrBr₃ sample was investigated in a dry cryogenic system at 1.6 K. The laser light was focused with a microscope objective down to a spot of about 1 μm. The sample was mounted on a piezo-stage that allowed *x*-*y*-*z* positioning. The light emitted from the sample was collected through the same objective and dispersed by a 0.75 m spectrometer from the Teledyne Princeton Instruments equipped with 150 grooves/mm, and then detected using a CCD.

DFT calculations

The first-principles calculations were performed within the density functional theory (DFT) in the Vienna ab-initio simulation package (VASP)^{76–79}. The projector augmented wave (PAW) potentials and general gradient approximation (GGA) of Perdew–Burke–Ernzerhof (PBE)⁸⁰ with D3 van der Waals correction⁸¹ were used. Spin-orbit coupling was not included due to its insignificant impact on lattice relaxation and phonon dispersion in this compound, as shown by Pandey et al. in Ref.⁶⁴. The unit cell and atomic positions have been optimized until forces on atoms were lower than 10^{−5} eV/Å and stress tensor components were lower than 0.1 kbar. A plane wave basis set cutoff of 500 eV and a Γ -centered *k*-mesh 6×6×6 were sufficient to converge the lattice constants with precision of 0.001 Å. An energy tolerance of 10^{−8} eV was used to in self-consistent loop. The phonon dispersion was calculated using the finite displacement method as implemented in Phonopy package^{82,83}. 2 × 2 × 2 supercells were found to assure convergence of the phonon frequencies at Γ point. All the calculations were performed at temperature of 0 K.

Received: 19 December 2023; Accepted: 20 March 2024

Published online: 29 March 2024

References

- Jiang, S., Li, L., Wang, Z., Mak, K. F. & Shan, J. Controlling magnetism in 2D CrI₃ by electrostatic doping. *Nat. Nanotechnol.* **13**, 549–553. <https://doi.org/10.1038/s41565-018-0135-x> (2018).
- Huang, B. et al. Electrical control of 2D magnetism in bilayer CrI₃. *Nat. Nanotechnol.* **13**, 544–548. <https://doi.org/10.1038/s41565-018-0121-3> (2018).
- Gilbertini, M., Koperski, M., Morpurgo, A. F. & Novoselov, K. S. Magnetic 2D materials and heterostructures. *Nat. Nanotechnol.* **14**, 408–419 (2019).
- Soriano, D., Katsnelson, M. I. & Fernández-Rossier, J. Magnetic two-dimensional chromium trihalides: A theoretical perspective. *Nano Lett.* **20**, 6225–6234. <https://doi.org/10.1021/acs.nanolett.0c02381> (2020).
- Wang, Q. H. et al. The magnetic genome of two-dimensional van der Waals materials. *ACS Nano* **16**, 6960–7079 (2022).
- Jin, W. et al. Raman fingerprint of two terahertz spin wave branches in a two-dimensional honeycomb insulating ferromagnet. *Nat. Commun.* **9**, 5122. <https://doi.org/10.1038/s41467-018-07547-6> (2018).
- Vaclavkova, D. et al. Magnetoelastic interaction in the two-dimensional magnetic material MnPS₃ studied by first principles calculations and Raman experiments. *2D Mater.* **7**, 035030. <https://doi.org/10.1088/2053-1583/ab93e3> (2020).
- Yin, T. et al. Chiral phonons and giant magneto-optical effect in CrCr₂ 2D magnet. *Adv. Mater.* **33**, 2101618. <https://doi.org/10.1002/adma.202101618> (2021).
- Li, S. et al. Magnetic-field-induced quantum phase transitions in a van der Waals magnet. *Phys. Rev. X* **10**, 011075. <https://doi.org/10.1103/PhysRevX.10.011075> (2020).
- Jana, D. et al. Magnon gap excitations in van der Waals antiferromagnet MnPSe₃ (2023). [arXiv:2309.06866](https://arxiv.org/abs/2309.06866)
- Pawbake, A. et al. High-pressure tuning of magnon-polarons in the layered antiferromagnet FePS₃. *ACS Nano* **16**, 12656–12665. <https://doi.org/10.1021/acsnano.2c04286> (2022).
- McGuire, M. A. Crystal and magnetic structures in layered, transition metal dihalides and trihalides. *Crystals* **7**, 121 (2017).
- Mak, K. F., Shan, J. & Ralph, D. C. Probing and controlling magnetic states in 2D layered magnetic materials. *Nat. Rev. Phys.* **1**, 646–661. <https://doi.org/10.1038/s42254-019-0110-y> (2019).
- Zhang, Y. & Wu, X. Vanadium sulfide nanoribbons: Electronic and magnetic properties. *Phys. Lett. A* **377**, 3154–3157 (2013).
- Wu, H.-J. et al. Ferromagnetic vanadium disulfide vs 2D monolayers with high Curie temperature and high spin polarization. *Phys. Chem. Chem. Phys.* **25**, 10143–10154. <https://doi.org/10.1039/D3CP00377A> (2023).
- Takano, Y. et al. Magnetic properties and specific heat of MPS₃ (M=Mn, Fe, Zn). *J. Magn. Magn. Mater.* **272–276**, E593–E595 (2004). <https://www.sciencedirect.com/science/article/pii/S0304885303023473>. *Proceedings of the International Conference on Magnetism* (ICM, 2003).
- Lançon, D. et al. Magnetic structure and magnon dynamics of the quasi-two-dimensional antiferromagnet FePS₃. *Phys. Rev. B* **94**, 214407. <https://doi.org/10.1103/PhysRevB.94.214407> (2016).
- Min Zhang, J., Zhuang Nie, Y., Guang Wang, X., Lin Xia, Q. & Hua Guo, G. Strain modulation of magnetic properties of monolayer and bilayer FePS₃ antiferromagnet. *J. Magn. Magn. Mater.* **525**, 167687 (2021).
- Lee, J. et al. Structural and optical properties of single- and few-layer magnetic semiconductor CrPS₄. *ACS Nano* **11**, 10935–10944. <https://doi.org/10.1021/acsnano.7b04679> (2017).
- Peng, Y. et al. Magnetic structure and metamagnetic transitions in the van der Waals antiferromagnet CrPS₄. *Adv. Mater.* **32**, 2001200. <https://doi.org/10.1002/adma.202001200> (2020).
- Rybak, M. et al. Magneto-optical anisotropies of 2D antiferromagnetic MPX₃ from first principles (2023). [arXiv:2308.13109](https://arxiv.org/abs/2308.13109)
- Göser, O., Paul, W. & Kahle, H. Magnetic properties of CrSBr. *J. Magn. Magn. Mater.* **92**, 129–136 (1990).
- Wang, Y., Luo, N., Zeng, J., Tang, L.-M. & Chen, K.-Q. Magnetic anisotropy and electric field induced magnetic phase transition in the van der Waals antiferromagnet CrSBr. *Phys. Rev. B* **108**, 054401. <https://doi.org/10.1103/PhysRevB.108.054401> (2023).
- McGuire, M. A. et al. Magnetic behavior and spin-lattice coupling in cleavable van der Waals layered CrCl₃ crystals. *Phys. Rev. Mater.* **1**, 014001. <https://doi.org/10.1103/PhysRevMaterials.1.014001> (2017).
- Serri, M. et al. Enhancement of the magnetic coupling in exfoliated CrCl₃ crystals observed by low-temperature magnetic force microscopy and X-ray magnetic circular dichroism. *Adv. Mater.* **32**, 2000566. <https://doi.org/10.1002/adma.202000566> (2020).
- Dillon, J. F. Jr. et al. Magneto-optical studies of chromium tribromide. *J. Appl. Phys.* **34**, 1240–1245 (1963).
- Dillon, J., Kamimura, H. & Remeika, J. Magneto-optical properties of ferromagnetic chromium trihalides. *J. Phys. Chem. Solids* **27**, 1531–1549 (1966).

28. McGuire, M. A., Dixit, H., Cooper, V. R. & Sales, B. C. Coupling of crystal structure and magnetism in the layered, ferromagnetic insulator CrI₃. *Chem. Mater.* **27**, 612–620. <https://doi.org/10.1021/cm504242t> (2015).
29. Li, S. *et al.* Magnetic-field-induced quantum phase transitions in a van der Waals magnet. *Phys. Rev. X* **10**, 011075. <https://doi.org/10.1103/PhysRevX.10.011075> (2020).
30. Wang, H., Eyert, V. & Schwingschlögl, U. Electronic structure and magnetic ordering of the semiconducting chromium trihalides CrCl₃, CrBr₃, and CrI₃. *J. Phys. Condens. Matter* **23**, 116003. <https://doi.org/10.1088/0953-8984/23/11/116003> (2011).
31. Yao, F. *et al.* Multiple antiferromagnetic phases and magnetic anisotropy in exfoliated CrBr₃ multilayers. *Nat. Commun.* **14**, 4969. <https://doi.org/10.1038/s41467-023-40723-x> (2023).
32. Lee, C. *et al.* Anomalous lattice vibrations of single- and few-layer MoS₂. *ACS Nano* **4**, 2695–2700. <https://doi.org/10.1021/nn1003937> (2010).
33. Grzeszczyk, M. *et al.* Raman scattering of few-layers MoTe₂. *2D Mater.* **3**, 025010. <https://doi.org/10.1088/2053-1583/3/2/025010> (2016).
34. Kipczak, L., Grzeszczyk, M., Olkowska-Pucko, K., Babinski, A. & Molas, M. R. The optical signature of few-layer ReSe₂. *J. Appl. Phys.* **128**, 044302. <https://doi.org/10.1063/5.0015289> (2020).
35. Bhatnagar, M. *et al.* Temperature induced modulation of resonant Raman scattering in bilayer 2H-MoS₂. *Sci. Rep.* **12**, 14169. <https://doi.org/10.1038/s41598-022-18439-7> (2022).
36. Wu, J. *et al.* Spin-phonon coupling in ferromagnetic monolayer chromium tribromide. *Adv. Mater.* **34**, 2108506 (2022).
37. Grzeszczyk, M. *et al.* Strongly correlated exciton-magnetization system for optical spin pumping in CrBr₃ and CrI₃. *Adv. Mater.* **35**, 2209513. <https://doi.org/10.1002/adma.202209513> (2023).
38. Li, H., Ruan, S. & Zeng, Y.-J. Intrinsic van der Waals magnetic materials from bulk to the 2D limit: New frontiers of spintronics. *Adv. Mater.* **31**, 1900065. <https://doi.org/10.1002/adma.201900065> (2019).
39. Craco, L., Carara, S. S., Shao, Y.-C., Chuang, Y.-D. & Freelon, B. Electronic structure of rhombohedral CrX₃ (X = Br, Cl, I) van der Waals crystals. *Phys. Rev. B* **103**, 235119. <https://doi.org/10.1103/PhysRevB.103.235119> (2021).
40. Mi, B.-Z. & Gu, Q. Two-dimensional intrinsic ferromagnetism in CrBr₃ monolayer. *Phys. Lett. A* **480**, 128980 (2023).
41. Kozlenko, D. P. *et al.* Spin-induced negative thermal expansion and spin-phonon coupling in van der Waals material CrBr₃. *npj Quantum Mater.* **6**, 19. <https://doi.org/10.1038/s41535-021-00318-5> (2021).
42. McGuire, M. A., Dixit, H., Cooper, V. R. & Sales, B. C. Coupling of crystal structure and magnetism in the layered, ferromagnetic insulator CrI₃. *Chem. Mater.* **27**, 612–620. <https://doi.org/10.1021/cm504242t> (2015).
43. Bermudez, V. M. Unit cell vibrational spectra of chromium trichloride and chromium tribromide. *Solid State Commun.* **19**, 693–697 (1976).
44. Lis, O. *et al.* Structural, magnetic and vibrational properties of the van der Waals ferromagnet CrBr₃ at high pressure. *Materials* **16**, 454 (2023).
45. Zhang, X. *et al.* Phonon and Raman scattering of two-dimensional transition metal dichalcogenides from monolayer, multilayer to bulk material. *Chem. Soc. Rev.* **44**, 2757–2785. <https://doi.org/10.1039/C4CS00282B> (2015).
46. Carvalho, B. R., Malard, L. M., Alves, J. M., Fantini, C. & Pimenta, M. A. Symmetry-dependent exciton-phonon coupling in 2D and bulk MoS₂ observed by resonance Raman scattering. *Phys. Rev. Lett.* **114**, 136403. <https://doi.org/10.1103/PhysRevLett.114.136403> (2015).
47. Kanazawa, K. K. & Street, G. B. The electrical properties of chromium tribromide. *Phys. Status Solidi B* **38**, 445–450 (1970).
48. Wood, D. L., Ferguson, J., Knox, K. & Dillon, J. F. Jr. Crystal-field spectra of d^{3,7} ions. iii. Spectrum of Cr³⁺ in various octahedral crystal fields. *J. Chem. Phys.* **39**, 890–898 (1963).
49. Jung, W. Dielectric constant and magneto-optical Kerr rotation of ferromagnetic chromium tribromide above the absorption band edge. *J. Appl. Phys.* **36**, 2422–2426 (1965).
50. Baral, D. *et al.* Small energy gap revealed in CrBr₃ by scanning tunneling spectroscopy. *Phys. Chem. Chem. Phys.* **23**, 3225–3232 (2021).
51. Acharya, S. *et al.* Real- and momentum-space description of the excitons in bulk and monolayer chromium tri-halides. *npj 2D Mater. Appl.* **6**, 33. <https://doi.org/10.1038/s41699-022-00307-7> (2022).
52. Guo, H. *et al.* Double resonance Raman modes in monolayer and few-layer MoTe₂. *Phys. Rev. B* **91**, 205415. <https://doi.org/10.1103/PhysRevB.91.205415> (2015).
53. Miranda, H. P. C. *et al.* Quantum interference effects in resonant Raman spectroscopy of single- and triple-layer MoTe₂ from first-principles. *Nano Lett.* **17**, 2381–2388. <https://doi.org/10.1021/acs.nanolett.6b05345> (2017).
54. Shcherbakov, D. *et al.* Raman spectroscopy, photocatalytic degradation, and stabilization of atomically thin chromium tri-iodide. *Nano Lett.* **18**, 4214–4219. <https://doi.org/10.1021/acs.nanolett.8b01131> (2018).
55. Wang, X., Sun, Y. & Liu, K. Chemical and structural stability of 2D layered materials. *2D Mater.* **6**, 042001 (2019).
56. Kim, S. *et al.* Crossover between photochemical and photothermal oxidations of atomically thin magnetic semiconductor CrP₃. *Nano Lett.* **19**, 4043–4051. <https://doi.org/10.1021/acs.nanolett.9b01417> (2019).
57. Mastrippolito, D. *et al.* Emerging oxidized and defective phases in low-dimensional CrCl₃. *Nanoscale Adv.* **3**, 4756–4766. <https://doi.org/10.1039/D1NA00401H> (2021).
58. Tu, Z. *et al.* Ambient effect on the Curie temperatures and magnetic domains in metallic two-dimensional magnets. *npj 2D Mater. Appl.* **5**, 62. <https://doi.org/10.1038/s41699-021-00242-z> (2021).
59. Wu, Y. *et al.* Degradation effect and magnetoelectric transport properties in CrBr₃ devices. *Materials* **15**, 3007 (2022).
60. Zhang, T. *et al.* Degradation chemistry and kinetic stabilization of magnetic CrI₃. *J. Am. Chem. Soc.* **144**, 5295–5303. <https://doi.org/10.1021/jacs.1c08906> (2022).
61. Liu, L. *et al.* Accelerated degradation of CrCl₃ nanoflakes induced by metal electrodes: Implications for remediation in nanodevice fabrication. *ACS Appl. Nano Mater.* **2**, 1597–1603. <https://doi.org/10.1021/acsanm.9b00058> (2019).
62. Webster, L. & Yan, J.-A. Strain-tunable magnetic anisotropy in monolayer CrCl₃, CrBr₃, and CrI₃. *Phys. Rev. B* **98**, 144411. <https://doi.org/10.1103/PhysRevB.98.144411> (2018).
63. Balkanski, M., Wallis, R. F. & Haro, E. Anharmonic effects in lattice scattering due to optical phonons in silicon. *Phys. Rev. B* **28**, 1928–1934. <https://doi.org/10.1103/PhysRevB.28.1928> (1983).
64. Pandey, T., Peeters, F. M. & Milošević, M. V. Pivotal role of magnetic ordering and strain in lattice thermal conductivity of chromium-trihalide monolayers. *2D Mater.* **9**, 015034. <https://doi.org/10.1088/2053-1583/ac427e> (2021).
65. Fennie, C. J. & Rabe, K. M. Magnetic and electric phase control in epitaxial EuTiO₃ from first principles. *Phys. Rev. Lett.* **97**, 267602. <https://doi.org/10.1103/PhysRevLett.97.267602> (2006).
66. Baltensperger, W. Influence of magnetic order on conduction electrons and phonons in magnetic semiconductors. *J. Appl. Phys.* **41**, 1052–1054. <https://doi.org/10.1063/1.1658810> (1970).
67. Lockwood, D. J. & Cottam, M. G. The spin-phonon interaction in FeF₂ and MnF₂ studied by Raman spectroscopy. *J. Appl. Phys.* **64**, 5876–5878. <https://doi.org/10.1063/1.342186> (1988).
68. Williams, T. J. *et al.* Magnetic correlations in the quasi-two-dimensional semiconducting ferromagnet CrSiTe₃. *Phys. Rev. B* **92**, 144404. <https://doi.org/10.1103/PhysRevB.92.144404> (2015).
69. Pawbake, A. *et al.* Raman scattering signatures of strong spin-phonon coupling in the bulk magnetic van der Waals material CrSBr. *Phys. Rev. B* **107**, 075421. <https://doi.org/10.1103/PhysRevB.107.075421> (2023).
70. Tian, Y., Gray, M. J., Ji, H., Cava, R. J. & Burch, K. S. Magneto-elastic coupling in a potential ferromagnetic 2D atomic crystal. *2D Mater.* **3**, 025035. <https://doi.org/10.1088/2053-1583/3/2/025035> (2016).

71. Luo, X., Zhao, Y., Zhang, J., Xiong, Q. & Quek, S. Y. Anomalous frequency trends in MoS₂ thin films attributed to surface effects. *Phys. Rev. B* **88**, 075320. <https://doi.org/10.1103/PhysRevB.88.075320> (2013).
72. Froehlicher, G. *et al.* Unified description of the optical phonon modes in n-layer MoTe₂. *Nano Lett.* **15**, 6481–6489. <https://doi.org/10.1021/acs.nanolett.5b02683> (2015).
73. Cheng, Z.-P., He, B.-G., Li, H. & Zhang, W.-B. Effect of thickness and stacking order on Raman spectrum of layered CrCl₃. *J. Phys. Condens. Matter* **33**, 355401. <https://doi.org/10.1088/1361-648X/ac0b1f> (2021).
74. Kazim, S. *et al.* Mechanical exfoliation and layer number identification of single crystal monoclinic CrCl₃. *Nanotechnology* **31**, 395706. <https://doi.org/10.1088/1361-6528/ab7de6> (2020).
75. Castellanos-Gomez, A. *et al.* Deterministic transfer of two-dimensional materials by all-dry viscoelastic stamping. *2D Mater.* **1**, 011002. <https://doi.org/10.1088/2053-1583/1/1/011002> (2014).
76. Kresse, G. & Hafner, J. Ab initio molecular dynamics for liquid metals. *Phys. Rev. B* **47**, 558–561. <https://doi.org/10.1103/PhysRevB.47.558> (1993).
77. Kresse, G. & Hafner, J. Ab initio molecular-dynamics simulation of the liquid-metal-amorphous-semiconductor transition in germanium. *Phys. Rev. B* **49**, 14251–14269. <https://doi.org/10.1103/PhysRevB.49.14251> (1994).
78. Kresse, G. & Furthmüller, J. Efficiency of ab-initio total energy calculations for metals and semiconductors using a plane-wave basis set. *Comput. Mater. Sci.* **6**, 15–50 (1996).
79. Kresse, G. & Furthmüller, J. Efficient iterative schemes for ab initio total-energy calculations using a plane-wave basis set. *Phys. Rev. B* **54**, 11169–11186. <https://doi.org/10.1103/PhysRevB.54.11169> (1996).
80. Kresse, G. & Joubert, D. From ultrasoft pseudopotentials to the projector augmented-wave method. *Phys. Rev. B* **59**, 1758–1775. <https://doi.org/10.1103/PhysRevB.59.1758> (1999).
81. Grimme, S., Antony, J., Ehrlich, S. & Krieg, H. A consistent and accurate ab initio parametrization of density functional dispersion correction (DFT-D) for the 94 elements H–Pu. *J. Chem. Phys.* **132**, 154104. <https://doi.org/10.1063/1.3382344> (2010).
82. Togo, A., Chaput, L., Tadano, T. & Tanaka, I. Implementation strategies in phonopy and phono3py. *J. Phys. Condens. Matter* **35**, 353001. <https://doi.org/10.1088/1361-648X/acd831> (2023).
83. Togo, A. First-principles phonon calculations with phonopy and phono3py. *J. Phys. Soc. Jpn.* **92**, 012001. <https://doi.org/10.7566/JPSJ.92.012001> (2023).

Acknowledgements

The work was supported by the National Science Centre, Poland (Grant No. 2020/37/B/ST3/02311), the Ministry of Education (Singapore) through the Research Centre of Excellence program (Grant EDUN C-33-18-279-V12, I-FIM) and under its Academic Research Fund Tier 2 (MOE-T2EP50122-0012), and the Air Force Office of Scientific Research and the Office of Naval Research Global under award number FA8655-21-1-7026. The calculations were carried out with the support of the Interdisciplinary Centre for Mathematical and Computational Modelling University of Warsaw (ICM UW) under computational allocation no G95-1773. T. W. acknowledge support from the National Science Centre Grant No. 2023/48/C/ST3/00309. K.W. and T.T. acknowledge support from the JSPS KAKENHI (Grant Numbers 21H05233 and 23H02052) and World Premier International Research Center Initiative (WPI), MEXT, Japan.

Author contributions

Ł.K. performed the measurements of the Raman scattering spectra. M.G. completed the PLE measurements. R.J. and T.W. carried out DFT calculations. Ł.K., A.K., and M.G. fabricated the samples with CrBr₃ thin flakes on the Si/SiO₂ substrates. Z.C. fabricated the sample of CrBr₃ encapsulated in hBN and covered by the polymer. T.T. and K.W. provide the hBN crystals. Ł.K., A.K., and J.P. carried out the AFM imaging. A.B. and M.R.M. participated in the measurements of the Raman spectra. M.K. and M.R.M. supervised the project. Ł.K. and M.R.M. analyzed the data. Ł.K., A.K., M.G., M.K. and M.R.M. wrote the manuscript with input from all coauthors.

Competing interests

The authors declare no competing interests.

Additional information

Correspondence and requests for materials should be addressed to Ł.K.

Reprints and permissions information is available at www.nature.com/reprints.

Publisher's note Springer Nature remains neutral with regard to jurisdictional claims in published maps and institutional affiliations.



Open Access This article is licensed under a Creative Commons Attribution 4.0 International License, which permits use, sharing, adaptation, distribution and reproduction in any medium or format, as long as you give appropriate credit to the original author(s) and the source, provide a link to the Creative Commons licence, and indicate if changes were made. The images or other third party material in this article are included in the article's Creative Commons licence, unless indicated otherwise in a credit line to the material. If material is not included in the article's Creative Commons licence and your intended use is not permitted by statutory regulation or exceeds the permitted use, you will need to obtain permission directly from the copyright holder. To view a copy of this licence, visit <http://creativecommons.org/licenses/by/4.0/>.

© The Author(s) 2024